

# Picomolar Fingerprinting of Nucleic Acid Nanoparticles Using Solid-State Nanopores

Mohammad Amin Alibakhshi,<sup>†,¶</sup> Justin R. Halman,<sup>§,¶</sup> James Wilson,<sup>¶,¶</sup> Aleksei Aksimentiev,<sup>\*,¶,¶</sup> Kirill A. Afonin,<sup>\*,§,⊥</sup> and Meni Wanunu<sup>\*,†,‡,¶</sup>

<sup>†</sup>Department of Physics and <sup>‡</sup>Department of Chemistry and Chemical Biology, Northeastern University, Boston, Massachusetts 02115, United States

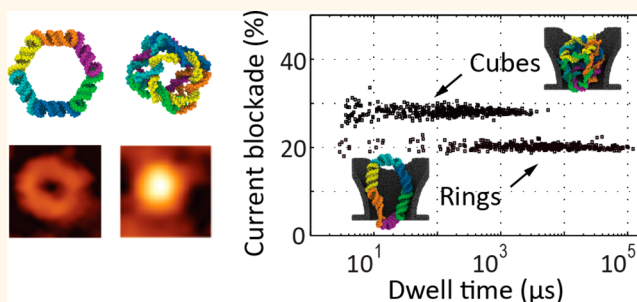
<sup>§</sup>Nanoscale Science Program, Department of Chemistry, and <sup>⊥</sup>The Center for Biomedical Engineering and Science, University of North Carolina at Charlotte, Charlotte, North Carolina 28223, United States

<sup>¶</sup>Department of Physics, University of Illinois at Urbana—Champaign, Urbana, Illinois 61801, United States

## Supporting Information

**ABSTRACT:** Nucleic acid nanoparticles (NANPs) are an emerging class of programmable structures with tunable shape and function. Their promise as tools for fundamental biophysics studies, molecular sensing, and therapeutic applications necessitates methods for their detection and characterization at the single-particle level. In this work, we study electrophoretic transport of individual ring-shaped and cube-shaped NANPs through solid-state nanopores. In the optimal nanopore size range, the particles must deform to pass through, which considerably increases their residence time within the pore. Such anomalously long residence times permit detection of picomolar amounts of NANPs when nanopore measurements are carried out at a high transmembrane bias. In the case of a NANP mixture, the type of individual particle passing through nanopores can be efficiently determined from analysis of a single electrical pulse. Molecular dynamics simulations provide insight into the mechanical barrier to transport of the NANPs and corroborate the difference in the signal amplitudes observed for the two types of particles. Our study serves as a basis for label-free analysis of soft programmable-shape nanoparticles.

**KEYWORDS:** nucleic acid nanoparticles, nanopore sensing, RNA and DNA nanotechnology, RNA ring, DNA cube



The advent of nanopores as a single-molecule platform has advanced studies of a wide range of species such as proteins, drugs, nucleotides, and polymers such as RNA, DNA, polypeptides, and polysaccharides.<sup>1–7</sup> Voltage-driven passage of analytes through a nanopore results in transient occlusion of the pore, which temporarily reduces the ionic current. The depth, duration, and frequency of the current modulations contain information about size,<sup>8–10</sup> charge,<sup>10,11</sup> and structure<sup>12,13</sup> of biomolecules and their interactions with the nanopore.<sup>3,14</sup> Deciphering such ionic current signals enables biophysical characterization of single-molecule processes<sup>15,16</sup> and contributes to development of single-molecule analytical methods<sup>16–19</sup> such as nanopore DNA sequencing.<sup>2,20–23</sup> Alongside the development of nanopore-based sensing techniques, advances in nucleic acid nanotechnology have enabled design and programming of complex molecular structures for applications in nanomedicine and nanobiotechnology.

Nucleic acid nanoparticles (NANPs) are self-assembled nanostructures composed of multiple RNA or DNA molecules.<sup>24</sup> To date, a variety of distinct NANPs has been

demonstrated differing from one another by their shape, size, internal connectivity, and physicochemical properties.<sup>24–47</sup> Ongoing development of NANPs is motivated by their potential applications in medicine and biotechnology, including their uses as carriers for RNAi inducers,<sup>47–50</sup> aptamers,<sup>48,51</sup> fluorophores, and as customizable materials.<sup>52–54</sup> Striking features of these nanoparticles are their precisely defined molecular structures, chemical stability, and tunable physicochemical properties. Moreover, due to their size uniformity and biocompatibility, NANPs are expected to outperform their metal and polymeric nanoparticle counterparts previously used for biosensing through antibody decoration, peptide coating, as well as DNA conjugation.<sup>55–58</sup>

In this work, we show that solid-state nanopores can be used to detect and characterize NANPs with high efficiency and precision. Akin to nanopore transport of deformable hydrogels,<sup>59–61</sup> nanopore transport of hollow and flexible NANPs

Received: July 12, 2017

Accepted: August 25, 2017

Published: August 25, 2017

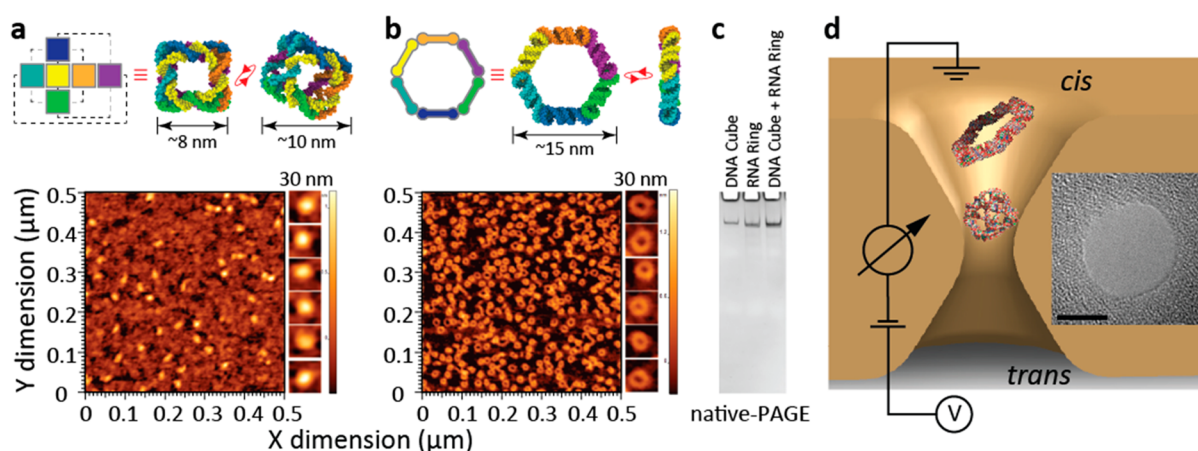


**Figure 1.** Assembly and visualization of nucleic acid nanoparticles (NANPs). Cartoon and 3D models (each strand colored differently) that define the structure of DNA cubes (a) and RNA rings (b). Below each structure, AFM images of the assembled structures are shown. (c) Ethidium bromide total staining native-PAGE of rings, cubes, and mixture of rings and cubes. (d) Schematics of a nanopore drawn approximately to scale with the two NANPs. Inset: Transmission electron micrograph of a 9 nm pore fabricated using electron beam irradiation of a 50 nm thick silicon nitride membrane (scale bar: 5 nm).

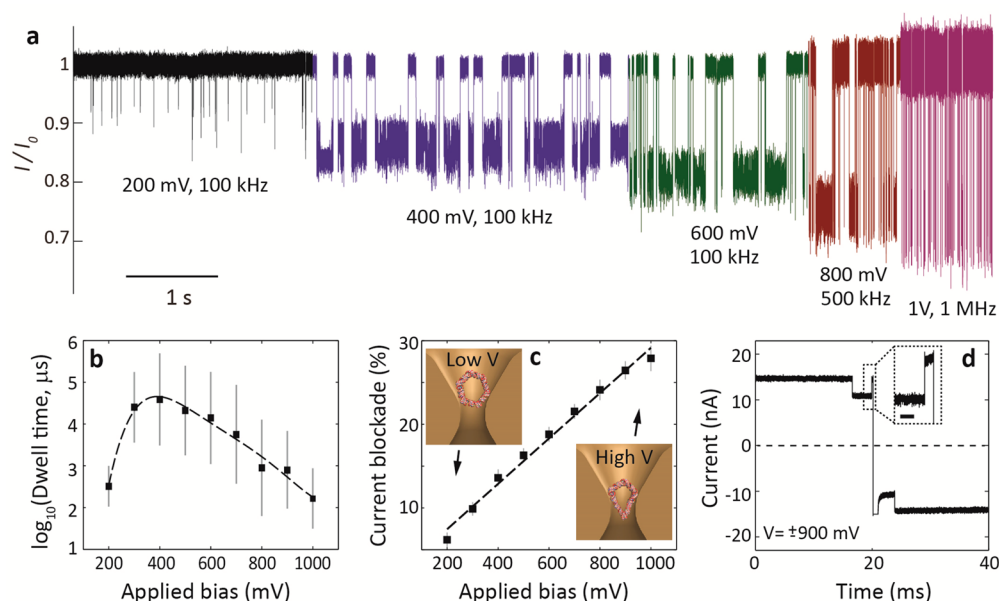


**Figure 2.** Deformation-controlled transport of NANPs. (a) Normalized current traces obtained for RNA rings interacting with a 9 nm nanopore at 200, 400, 600, 800, and 1000 mV (for 400 and 600 mV data, open-pore segments were excised to allow more events to be seen). (b) Mean dwell time *versus* applied bias for RNA rings (dashed line is a trendline fit to the eye). Vertical lines for each data point represent  $\pm 1$  standard deviation in the corresponding dwell time distributions. (c) Mean fractional blockade *versus* applied bias (dashed line is a linear fit). Inset cartoons are perceived interpretations of the increasing fractional blockades with increasing voltage. (d) Recapture of an RNA ring. Switching polarity of the voltage bias immediately after a long ionic current blockade produced a similar amplitude opposite polarity blockade event, confirming nanopore translocation of NANPs and further suggesting that NANPs retain their structure after translocation (inset scale bar: 300  $\mu$ s). Experiments performed with 400 mM KCl (10 mM Tris, 2 mM MgCl<sub>2</sub>, pH 7.9).

can be expected to report on their mechanical properties. Furthermore, distinguishing individual types of NANPs *via* a nanopore measurement can enable multiplexed detection of biomarkers using functional NANPs. Here, we characterize nanopore translocation of ring-shaped RNA and cube-shaped DNA nanoparticles and find that mechanical deformation of NANPs governs their passage through narrow pores. Next, we examine the detection limit of such nanopore measurements and show that individual particles from a binary mixture can be identified based on an ionic current pulse produced by a single nanopore passage of a nanoparticle.

## RESULTS AND DISCUSSION

In this work, we explore nanopore transport of NANPs using two representative NA structures that are further referred to as DNA cubes and RNA rings. Each structure is composed entirely of either DNA or RNA strands, self-assembled according to the prescribed connectivity rules. The DNA cubes<sup>47</sup> are assembled through intermolecular canonical Watson–Crick base pairing, whereas the RNA rings<sup>62</sup> are formed *via* RNA–RNA tertiary interactions known as kissing loops.<sup>63</sup> To initiate the magnesium-dependent kissing loop interactions, individual monomers of RNA rings must be

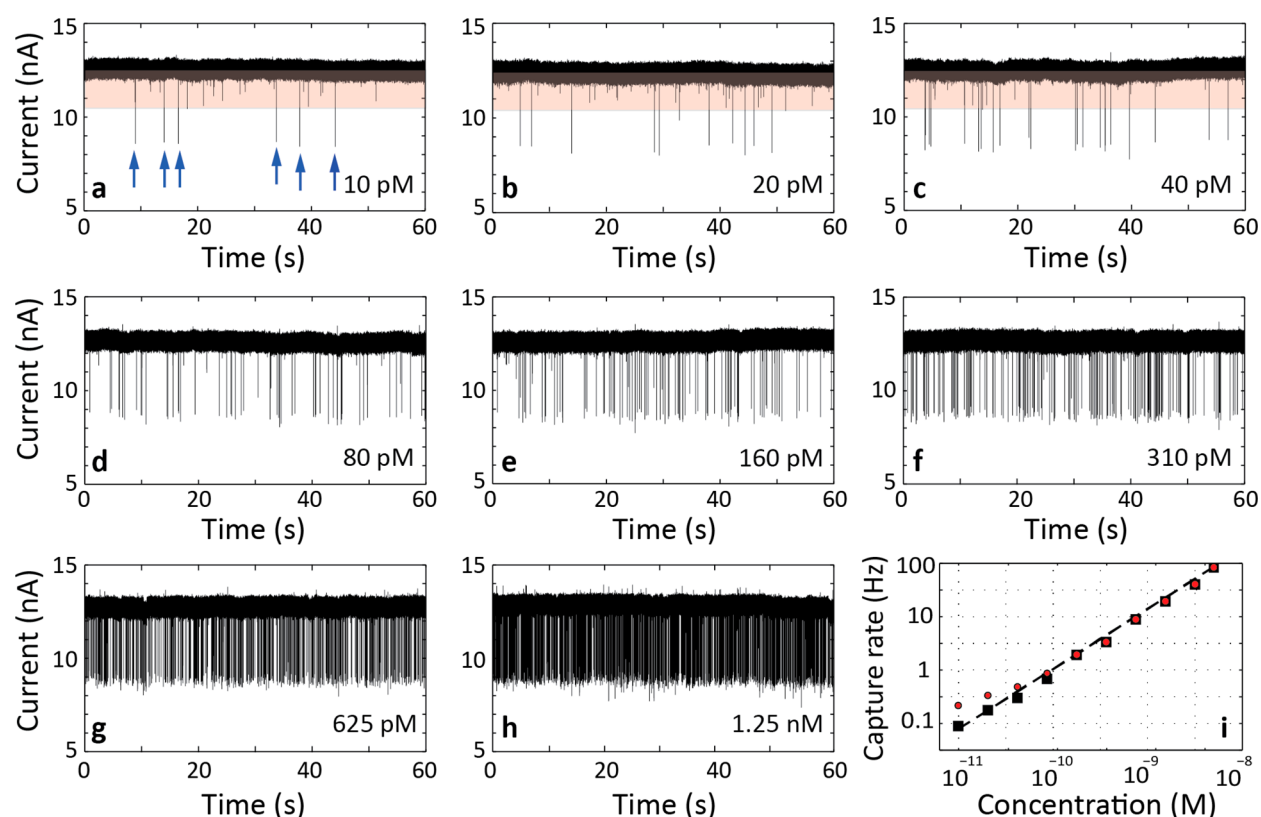


**Figure 3.** Concentration limit of NANP detection. (a–h) Current traces recorded from samples containing RNA rings at different concentrations. All measurements were carried out using a 9 nm pore at 1 V applied bias; the data were low-pass filtered at 500 kHz. Shaded regions in panels a–c highlight occurrence of shallow events. (i) Capture rate *versus* concentration of RNA rings. Red markers: capture rate based on total number of events. Black markers: capture rate after omission of the shallow events with fractional blockade less than 15%. Experiments performed with 400 mM KCl (10 mM Tris, 2 mM MgCl<sub>2</sub>, pH 7.9).

prefolded prior to assembly. In contrast, monomers entering the composition of DNA cubes were designed to avoid any internal secondary structures.

To assess the physical characteristics of these NANPs, we used atomic force microscopy (AFM) (Figure 1a,b) and gel electrophoresis (Figure 1c), both of which show the formation of monodisperse and highly regular structures. Our nanopore setup is schematically shown in Figure 1d. The nanopore forms a solitary electrolyte contact between the *cis* and *trans* side of the membrane. Applying an electric field across the pore produces a steady-state ion current as well as a localized electric field that captures and drives charged nanoparticles through the pore. Each time a nanoparticle interacts with the pore, the ion flux through the pore is reduced transiently, producing an electrical spike.

Previously, increasing the electric field was found to facilitate nanopore capture of biomolecules from the bulk solution and increase the signal-to-noise ratio of the produced electrical spikes.<sup>64,65</sup> A major downside, however, was the shorter duration of the nanopore translocation process, which compromised detection efficiency. In the case of NANPs, however, we find that it is possible to increase the capture rate without compromising the detection efficiency. Employing pores with diameters in the range of 9–10 nm, just smaller than the size of a NANP, forces NANPs to reside at the nanopore entrance for a prolonged time before being squeezed through the nanopore by the electric field. As a result, every particle is detected with high signal-to-noise ratio using high-bandwidth electronics.<sup>66</sup>

Sample current traces for RNA rings through a 9 nm pore at different applied voltages are shown in Figure 2a. The current is normalized by its open-pore value to highlight changes in the fractional blockade. We find that the fractional current blockade increases with applied bias. Further, we observe a seemingly counterintuitive result of longer dwell times at 400 mV than at 200 mV bias, which defies the previously observed trends in translocation of DNA<sup>64</sup> and proteins<sup>65</sup> through nanopores. Increasing the applied bias beyond 400 mV reveals the trend expected with translocation, namely, faster dwell times with increasing voltage. We rationalize these results as follows: below a certain voltage threshold, the RNA rings only collide with the pore and do not translocate because the electromotive force that drives the NANPs is insufficient for squeezing them through. As a result, the NANPs dwell in the pore entrance for durations that span orders of magnitude. Beyond a certain threshold defined by the electric field strength, the NANPs traverse the pore. A similar mechanism was previously suggested to govern transport of double-stranded DNA through very narrow pores in silicon nitride membranes,<sup>67</sup> as well as the docking translocation of DNA origami nanoplates in 5–30 nm nanopores.<sup>68</sup> The deformation-controlled mechanism of NANP translocation is also borne out by the observation of increasing fractional blockades with voltage (Figure 2c), which reports on how deep the NANPs enter into the pore constriction. The transition from collisions to translocations manifests itself in Figure 2b as a peak in the dwell times at ~400 mV, although we find the exact location of the peak to depend on the pore and particle geometry. Another example of

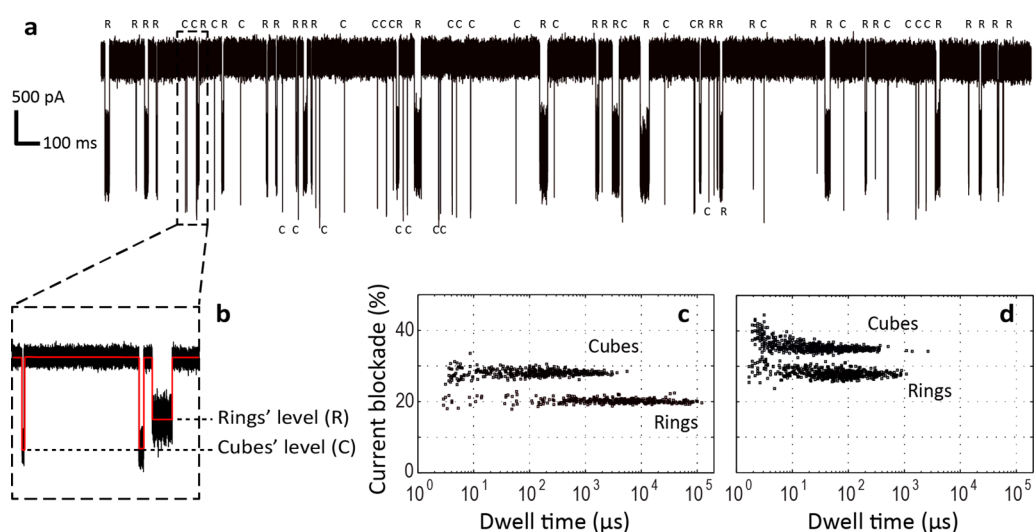


**Figure 4.** Discrimination of RNA rings from DNA cubes. (a) Current traces measured from a binary mixture of DNA cubes and RNA rings (1 nM ring; 1.4 nM cube). The translocation experiments were performed using a 9.5 nm diameter pore, with a 500 mV transmembrane voltage; data were low-pass filtered at 500 kHz. (b) Close view of the current trace indicates two distinct blockade levels associated with each nucleic acid nanoparticle. (c) Scatter plot of the fractional blockade versus dwell time measured at 500 mV applied bias displays two distinct populations corresponding to the DNA cubes ( $n = 422$ ) and the RNA rings ( $n = 376$ ). (d) Scatter plot similar to (c) obtained at an applied bias of 800 mV. In this panel, data were processed using a 1 MHz low-pass filter ( $n_{\text{cube}} = 573$ ,  $n_{\text{ring}} = 498$ ). Experiments performed with 400 mM KCl (10 mM Tris, 2 mM  $\text{MgCl}_2$ , pH 7.9).

dwell time dependence is shown in [Supporting Information \(SI\) Figure S1](#), where the peak voltage is at  $\sim 700$  mV. Note that the nanopore shape drawn in [Figure 1d](#) is derived from the prior tomography-based studies of pores produced using a similar fabrication protocol.<sup>69,70</sup> Thus far, our results suggest that nanopore translocation of NANPs involves processes that occur at two separate time scales: the dwell time scale associated with NANPs residing at the nanopore entrance and the passage time scale associated with actual nanopore translocation of NANPs. Whereas the dwell times of the RNA rings span several orders of magnitude (see [SI Figure S1](#) and [Figure 4c,d](#)), the passage times are expected to be much shorter than the dwell times, given that the nanopore translocation can only happen after deformation and/or buckling of the stalled nanoparticles. Thus, although we would expect to see deeper blockades when NANPs pass through the pores, we do not detect them presumably due to the passage time scales shorter than those detectable by our electronics ( $>1$   $\mu\text{s}$  detection limits).

In order to verify successful translocation of NANPs through the nanopore, we performed nanopore recapture experiments (see [Figure 2d](#)).<sup>71</sup> In these experiments, a transition in the pore current level from the NANP-occupied state back to the open state triggers the hardware to reverse the bias polarity after a set delay, which we have chosen to be 200  $\mu\text{s}$ . Such rapid switching of bias polarity results in recapture of the same NANP that just passed through the nanopore. Recapture of the rings, which occurs with a probability of  $\sim 10\%$ , validates our interpretation of long-lasting blockades as NANP capture terminated by nanopore translocation. Furthermore, ionic current blockades produced by both translocation and recapture are very similar (more example events are shown in [SI Figure S2](#)), with slight variations in the exact signal amplitude and durations ( $<20\%$ ) that may be accounted for by the nanopore-shape asymmetry. This finding suggests that nanopore translocation does not disrupt the structural integrity of the rings, as linear RNA molecules of similar mass are not expected to produce signals of

similar amplitudes and durations given that the translocation kinetics of a NANP is conditioned by both the size of the ring and its mechanical compliance.

In a typical nanopore experiment, the voltage applied across the pore serves to facilitate the capture of analytes as well as to translocate them through the pore. Therefore, capture and translocation are coupled, which makes detection of trace amounts of analyte challenging. Indeed, although detection limits for a particular analyte can be increased by increasing the applied bias,<sup>72</sup> any increase in applied bias would also speed up the translocation process, which usually compromises detection. However, in contrast to free translocation of particles through nanopores that are larger than the analytes, in the regime of deformation-controlled transport, capture and translocation can be decoupled. In [Figure 3a–h](#), we show example 60 s current traces for RNA rings at 1 V applied bias for concentrations ranging from 10 pM to 1.25 nM. The experiment was carried out by serial dilution (2 $\times$ ) of a 5 nM solution of RNA rings, followed by recording of  $\sim 150$  s of data at each concentration for mean capture rate calculation. [Figure 3i](#) displays a log–log plot of the mean capture rate of the RNA rings as a function of their concentration. Red markers were obtained by calculating the capture rate based on the total number of recorded events, whereas the black markers represent capture rates for only events with amplitudes that are larger than 15% of the open-pore current (mean blockades of rings  $\sim 30\%$ ). With the shallow events omitted, a power law fit to the log–log data yields a power of 1.12, which closely matches the expected linearity (1.0 power), the discrepancy either stemming from volume estimation error or from pipet miscalibration. However, it is noteworthy that omitting the random (and rare) shallow events that result either from pore surface contamination or from buffer contamination allows us to push detection limits to the pM levels. Finally, we have calculated the capture radius of the rings from the observed capture rates, yielding values of  $\sim 100$  nm; the diffusion coefficient of an RNA ring was estimated to be 40  $\mu\text{m}^2/\text{s}$  using

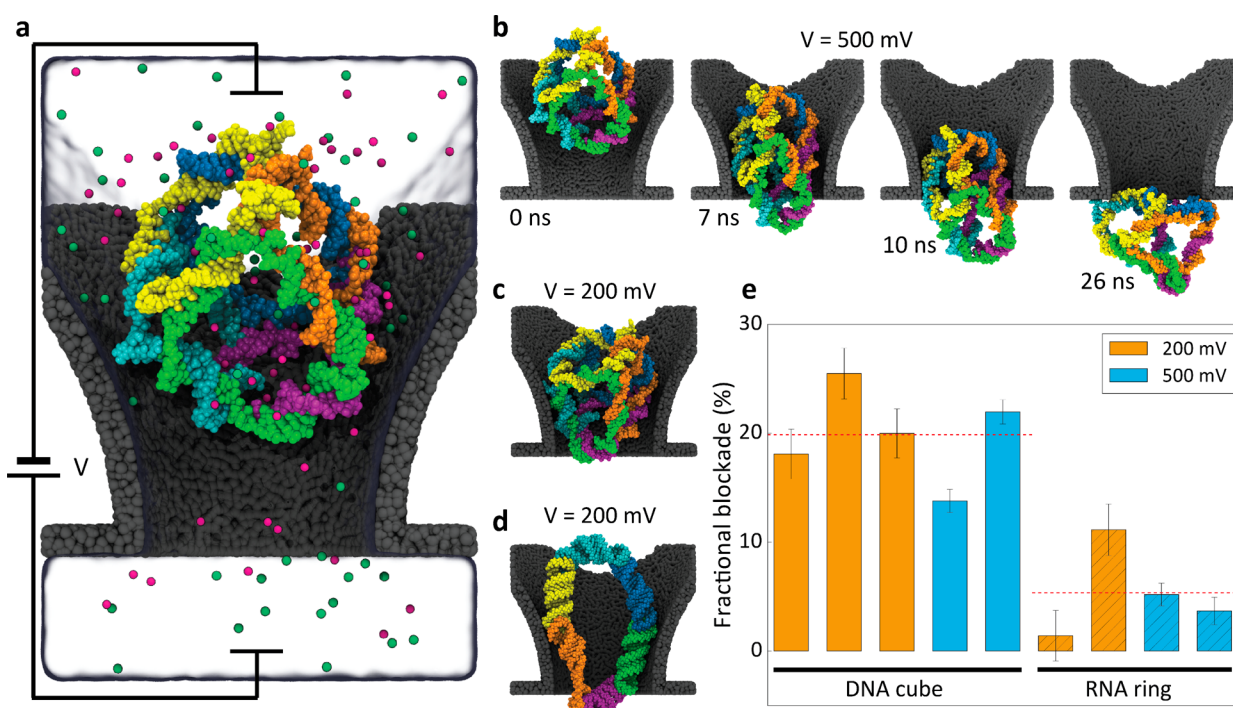


**Figure 5.** MD simulations of NANPs' translocation through a solid-state nanopore. (a) Typical simulation system containing a nanopore (gray), a DNA cube (colors), water (semitransparent surface), and ions (spheres). The diameter of the nanopore constriction is 9 nm. (b) Snapshots illustrating a simulated translocation of a DNA cube under a 500 mV transmembrane bias. Water and ions are not shown for clarity. (c,d) Representative conformations of a DNA cube (c) and an RNA ring (d) trapped at the nanopore constriction under a 200 mV transmembrane bias. (e) Percentage of the open-pore current reduced by the nanoparticles trapped in the nanopore. Several independent simulations were performed for each particle at each bias condition differing by the initial orientation of the particles with respect to the nanopore (see SI Figure S6). The blockade currents were determined after the particles reached a stable conformation within the nanopore (see SI Figure S7 and Table S1). The error bars represent the propagated standard error of 800 ps block averaging. A horizontal dashed line denotes the average blockade currents produced by DNA cubes and RNA rings.

the nominal size of the ring and the Einstein–Stokes equation. We note that for a previous study of double-stranded DNA capture into small (4 nm diameter) nanopores,<sup>72</sup> the capture radius was found to be commensurate with the DNA radius of gyration. In contrast, the higher voltages used in our experiment, coupled to high efficiency detection that results from deformation-controlled transport, yields a capture radius for the deformable structure that is an order of magnitude larger than its radius of gyration.

After having characterized the nanopore transport of RNA rings, we have carried out similar measurement using DNA cubes (see Figure 1 and SI Figure S3). Overall, DNA cubes exhibit very similar transport behavior, including very broad dwell time distributions, increased fractional blockade with increasing voltage, and nonmonotonous behavior of dwell times with increasing voltage values. A simple theoretical estimate of the fractional blockade produced by a DNA cube is in good agreement with the results of our measurements (see SI, section III). Owing to their 3D structure, DNA cubes can block a larger volume of the pore in its high electric field zone, hence causing larger current blockades. This permits the use of the same pore to discriminate DNA cubes from RNA rings. Figure 4a directly shows the possibility of such shape differentiation. Clearly, two distinct blockade levels are present in the trace, as further exemplified in the close-up of Figure 4b. Experiments conducted with individual NANPs as well as their binary mixtures (1 nM ring; 1.4 nM cube) confirmed that the higher-level blockade belongs to the cubes (see Figure S4). The scatter plot of the fractional blockade *versus* dwell time clearly

demonstrates two mutually exclusive populations, indicating that cubes and rings can be differentiated based on single pulses with  $\geq 99\%$  efficiency (Figure 4c). In other words, each event in the scatter plot can be mapped to either a ring or a cube, based on its fractional blockade amplitude. Given that both particles deform as they enter the pore constriction, increasing the applied bias to 800 mV results in increased fractional current blockades for both NANPs while also reducing their corresponding mean dwell times (Figure 4d). These results were reproduced using 15 different nanopores in the  $9.5 \pm 1$  nm range at different applied voltages despite small variabilities in the fractional current blockades and translocation threshold voltage that are related to the exact nanopore geometry. It is important to note that in the gel electrophoresis experiment performed using a ring–cube mixture (Figure 1c), the two types of NANPs, despite being different in shape and size, migrate very similarly and hence are difficult to distinguish from one another. In contrast, the deformation-controlled transport through nanopores enables accurate differentiation of the two NANP species. An even more accurate quantification of a composition of a NANP mixture, in addition to measuring the capture rate, would require accounting for the relative capture probability for each nanoparticle, which in practice would reduce to a calibration measurement for each particle type.

To elucidate the microscopic mechanism of NANP permeation through solid-state nanopores and to obtain an independent assessment of the ionic current blockade levels, we constructed several all-atom models of a nanopore system containing either a DNA cube or an RNA ring nanoparticle

(Figure 5a). To increase the computational efficiency of molecular dynamics (MD) simulations, the nanopore shape was chosen to reproduce the *cis* half of the experimental nanopore system, with the *trans* side cut off at the membrane midplane. Prior to simulations of the nanopore transport, the nanoparticles were equilibrated for at least 60 ns in bulk 400 mM KCl solution until their root-mean-square deviation (rmsd) from the idealized geometry had reached steady values of 1.2 and 0.6 nm for the DNA cube and the RNA ring, respectively (SI Figure S8). Such rather large equilibrium rmsd values reflect considerable structural fluctuations that nevertheless do not affect integrity of the particles. Indeed, more than 90% of all base pairs remained intact during the free equilibration simulation (SI Figure S8).

To simulate nanopore transport, equilibrated NANPs were placed at the opening of the nanopore (Figure 5a) and, following short equilibration, were simulated under a transmembrane bias of either 200 or 500 mV. Several independent simulations were performed at each bias; Table S1 provides a summary of all MD runs. In some simulations performed at a 500 mV bias, the particles were observed to pass through the nanopore constriction, rapidly exiting on the *trans* side; one such trajectory is featured in Figure 5b. Interestingly, the DNA cube maintained its integrity after the translocation (SI Figure S9). In the majority of the simulations, however, the particles became wedged at the *cis* entrance of the nanopore. Two such stable conformations are shown in Figure 5c,d; SI animations 1–5 represent simulation trajectories. Once the structures had reached an equilibrium conformation and their movement effectively ceased, see SI Figure S7 and Table S1, we calculated the ionic current for each of the structures directly from the motion of the ions through the nanopore. For comparison, we also simulated the ionic current through the nanopore containing no nanoparticles. Figure 5e plots the current blockade percentage  $100(I_0 - I)/I_0$ , where  $I$  is the ionic current passing through the nanopore and  $I_0$  is the open-pore current. The DNA cube blocked a higher percentage of the current than the RNA ring in our simulations, at both biases, which is in agreement with our experimental data. Note that, because of the difference in the geometry of the simulated and experimental nanopore systems, the simulations systematically underestimate the fractional blockade levels.

## CONCLUSIONS

NANPs have shown promise as enablers of advanced biophysical studies and as probes for molecular sensing approaches. Here, we have used measurements of ionic current to characterize the process of NANPs' transport through solid-state nanopores, identifying conditions where deformability of the nanoparticles determines their transport characteristics. Specifically, we find that elastic deformation of NANPs in response to the applied electric field permits them to pass through nanopores smaller than the particle size but only after the force on the particles in the nanopore exceeds a threshold value. Such deformation results in longer dwell times, which considerably improves NNP detection limits even at a high applied bias. Furthermore, nanoparticles of different types (*i.e.*, RNA rings and DNA cubes) produce distinct populations of ionic current blockade, and the type of individual particle transiting a nanopore from a particle mixture can be determined from a single current blockade. Such a tremendous distinguishability, combined with picomolar sensitivity, poises nanopore-based sensing of NANPs as an attractive candidate

for development of a multiplexed detection platform for general biomarker sensing. Finally, our work introduces nanopores as sensitive tools for investigation of the physical properties of multistrand nanoassemblies, which are challenging to characterize otherwise, especially when several nanoparticle types of comparable sizes, charges, and molecular weights are simultaneously present in the mixture, even at pM concentrations.

## METHODS

**Nanoparticle Synthesis and Characterization.** All NANPs were assembled by combining individual monomer components at equimolar concentrations. The oligonucleotides encoding the composition of NANPs are listed in the Supporting Information. DNA oligonucleotides were purchased from IDT ([idtdna.com](http://idtdna.com)), and RNA strands were produced by *in vitro* runoff transcription using PCR-amplified DNA templates. For that, synthetic DNAs coding for the sequence of the designed RNA were amplified by PCR using primers containing the promoters for T7 RNA polymerase. PCR-amplified and purified (DNA Clean&Concentrator-5, Zymo Research) DNA templates (0.2  $\mu$ M) were transcribed with "home-made" T7 RNA polymerase in 80 mM HEPES-KOH, pH 7.5; 2.5 mM spermidine; 50 mM DTT; 25 mM MgCl<sub>2</sub>; 5 mM NTPs. Transcription was stopped with RQ1 DNase. Transcribed RNAs were purified with 8 M urea denaturing gel electrophoresis (PAGE, 15% acrylamide). The RNAs were eluted from gel slices overnight at 4 °C into 1× TBE buffer containing 300 mM NaCl and then precipitated in 2.5 volumes of 100% ethanol. Samples were then rinsed with 90% ethanol, vacuum-dried, and dissolved in double-deionized water.

For assembly of DNA cubes, corresponding oligonucleotides (purchased from IDT) were mixed in doubly deionized water, heated to 95 °C for 2 min, snap-cooled to 45 °C, and incubated for 20 min. For assembly of RNA rings, mixtures of RNAs (individually transcribed and purified) were heated to 95 °C for 2 min, followed by snap-cooling on ice for 2 min, and incubation at 30 °C for 30 min. An assembly buffer (1× concentration: 89 mM tris-borate (pH 8.3), 2 mM MgCl<sub>2</sub>, 50 mM KCl) was added following the heating step to all assemblies.

All NANPs were characterized by the electrophoretic mobility shift assays carried out on 8% nondenaturing native PAGE (37.5:1, 2 mM MgCl<sub>2</sub>) and visualized with a Bio-Rad ChemiDoc MP system using total staining with ethidium bromide (EtBr). All gels were run for 30 min at 4 °C, 300 V. NANPs were further visualized by AFM. For that, 5  $\mu$ L of 50 nM NANPs was deposited on APS-modified mica, incubated for ~2 min, and air-dried, as described previously. AFM visualization was carried out in tapping mode on a MultiMode AFM Nanoscope IV system (Bruker Instruments, Santa Barbara, CA). The images were recorded with a 1.5 Hz scanning rate using a TESPA-300 probe from Bruker with a resonance frequency of 320 kHz and spring constant of about 40 N/m. Images were processed by the FemtoScan Online software package (Advanced Technologies Center, Moscow, Russia).<sup>73,74</sup>

**Nanopore Fabrication and Measurement.** The nanopore devices are 5 × 5 mm<sup>2</sup> chips with a 50 nm thick freestanding silicon nitride membranes at the center. Nanopores were drilled using a JEOL 2010F transmission electron microscope operating at 200 kV. After fabrication, nanopore chips were cleaned using hot Piranha (sulfuric acid/hydrogen peroxide, 2:1), rinsed first by hot DI water and then by a stream of DI water, and finally dried under a gentle stream of nitrogen. Next, the chips were mounted in a custom PTFE cell, and a fast-curing silicone elastomer was used to seal the edges as well as to paint the exposed areas of the chips as close as possible to the membrane. This painting along with a 2  $\mu$ m thick silicon oxide layer intermediating the silicon substrate and the silicon nitride layer reduced the capacitive noise of these chips, allowing high bandwidth electrical measurement of the ionic current through the nanopore. The rms noise of the chips after filtering with a 1 MHz low-pass filter was in the range of 180–220 pA. The fluidic cell is composed of two chambers (*cis* and *trans*) that can only be connected through the

nanopore. Experiments were performed with 400 mM KCl (10 mM Tris, 2 mM MgCl<sub>2</sub>, pH 7.9). This low concentration of Mg<sup>2+</sup> ions was added to the buffer to help with preserving the nanoparticles. The silver/silver chloride electrodes interface the fluidics with the electronics. The ionic current was recorded using a Chimera VC100 amplifier (Chimera Instruments LLC), digitized at 4.17 M sample/s and digitally low-pass filtered.

Before each experiment, the conductance of the nanopores was measured and compared against the theoretical values to confirm the dimensions of the nanopores. Next, the nanoparticles were added to the *cis* chamber (grounded), and a positive bias was applied to the *trans* chamber. Upon applying the bias, the charged nanoparticles were electrophoretically driven through the nanopore and the translocation events were observed in the form of spikes in the DC current. The height and width of these events, that is, current blockade by a nanoparticle and the dwell time of a nanoparticle in the nanopore contain information about the structure of the nanoparticles and their interactions with the nanopore. Additionally, the interevent time distribution (the time interval between two successive events) was used to determine the capture rate, which was then correlated with the concentration of nanoparticles. Pyth-Ion, a nanopore data analysis package, was used to extract such data from the recordings. Further analysis and distribution fittings were performed with MATLAB R2014.

**Molecular Dynamics Simulations.** All MD simulations of the NANPs/nanopore systems were carried out using NAMD2,<sup>75</sup> periodic boundary conditions, the CHARMM36 force field,<sup>76</sup> a custom force field for silica,<sup>77</sup> and the CUFIX corrections for ions.<sup>78</sup> Multiple timestepping<sup>79</sup> was used: local interactions were computed every 2 fs, whereas long-range interactions were computed every 6 fs. All short-range nonbonded interactions were cut off starting at 0.8 nm and completely cut off by 1.0 nm. Long-range electrostatic interactions were evaluated using the particle-mesh Ewald method<sup>80</sup> computed over a 0.1 nm spaced grid. SETTLE<sup>81</sup> and RATTLE<sup>82</sup> algorithms were applied to water and nucleic acid hydrogen atoms, respectively. A Langevin thermostat of 1.0 ps<sup>-1</sup> damping constant was coupled to silica atoms to maintain constant temperature. Atoms of silica membrane were also harmonically restrained to their initial coordinates; the spring constant of the restraints was 200 kcal mol<sup>-1</sup> Å<sup>-2</sup>. Constant pressure simulations employed a Nosé–Hoover Langevin piston.<sup>83</sup>

The atomic-scale model of a solid-state nanopore was obtained by annealing high-temperature (7000 K) silica melt in the presence of a grid-based potential that defined the shape of the nanopore. During the annealing simulation, the temperature of the system was set to 7000, 5000, 2000, and 300 K for 40 000, 40 000, 100 000, and 100 000 steps, respectively. These simulations were performed in vacuum using the BKS force field.<sup>84</sup> The nanopore shape was chosen to match the nanopore geometry realized in the experiment:<sup>70</sup> the nanopore had an hourglass shape with the middle section approximated by a 9 nm diameter cylinder and the nanopore entrances approximated by 30° angle cones. To reduce the cost of MD simulations, the nanopore shape was cut in half along the midplane of the membrane, resulting in an asymmetric system shown in Figure 4a. After being annealed, atoms located farther than 1 nm away from the nanopore surface were removed, further reducing the computational cost of the simulations.

Initial models of NA particles were built by arranging DNA and RNA strands according to the particle's idealized geometry. The cube and the ring particles were submerged in a cubic volume of 400 mM KCl electrolyte 14 and 18 nm on each side, respectively. The systems were equilibrated in the constant number of particles, pressure, and temperature (NPT) ensemble for over 60 ns each ( $P = 1$  atm;  $T = 295$  K). The equilibrated systems were then merged with the all-atom model of the nanopore, placing each NANP at the entrance of the nanopore with its center of mass initially located at the nanopore axis. The ring particle was initially oriented normal to the silica membrane. Three versions of the cube/nanopore system were built differing by the orientation of the cube with respect to the nanopore (SI Figure S6). Water and ions that clashed with the membrane were removed; additional volumes of 400 mM KCl solution were added to fully wet

the nanopore and to form water-filled compartments on either side of the membrane. The final systems measured  $16 \times 16 \times 23$  nm<sup>3</sup> and contained approximately 470 000 atoms. The systems were equilibrated in the NPT ensemble for approximately 5 ns. Following the equilibration, the simulations were run in the constant number of particles, volume, and temperature (NVT) ensemble. An external electric field,  $E = -V/L_z$ , was applied along the nanopore axis to produce the target drop of the electric potential,  $V$ , over the system's dimension in the direction of the applied field,  $L_z$ .<sup>85</sup> In all simulations, a short-range repulsive potential was applied to atoms of NANPs to prevent their permanent binding to the nanopore surface.<sup>86</sup>

## ASSOCIATED CONTENT

### Supporting Information

The Supporting Information is available free of charge on the ACS Publications website at DOI: 10.1021/acsnano.7b04923.

Compositions of the nanoparticles; translocation of the DNA cubes and RNA rings through a nanopore at different voltages; recapture of RNA rings at different voltages; estimation of the fractional current blockade; initial orientation of the NANPs in MD simulations; simulated displacement of NANPs through a nanopore; structural fluctuations of NANPs in bulk solution; structural integrity of NANPs during simulated nanopore translocation; animations illustrating MD trajectories of a DNA cube translocation through a solid-state nanopore with different initial orientations under a 200 mV bias, an MD trajectory of a DNA cube translocation under a 500 mV bias, an MD trajectory of an RNA ring translocation under a 200 mV bias translocation (PDF)

Animation M1 (MPG)

Animation M2 (MPG)

Animation M3 (MPG)

Animation M4 (MPG)

Animation M5 (MPG)

## AUTHOR INFORMATION

### Corresponding Authors

\*E-mail: aksiment@illinois.edu.

\*E-mail: kafonin@uncc.edu.

\*E-mail: wanunu@neu.edu.

### ORCID

Aleksei Aksimentiev: 0000-0002-6042-8442

Meni Wanunu: 0000-0002-9837-0004

### Author Contributions

†M.A.A., J.R.H., and J.W. contributed equally to this work.

### Notes

The authors declare no competing financial interest.

## ACKNOWLEDGMENTS

We thank Dr. Vivek Jadhav for fabricating the silicon nitride membrane chips, and Drs. Alexander Lushnikov and Alexey Krasnoslobodtsev for performing AFM imaging at the Nano-imaging core facility at the University of Nebraska Medical Center. We acknowledge the National Institutes of Health R01 HG009186 (M.A.A. and M.W.), R01-GM114204 and R01-HG007406 (A.A. and J.W.), the National Science Foundation NSF-1645671 (M.W.), DMR-1507985 (A.A.), and the UNCC Department of Chemistry start-up funds (K.A.A.). Super-computer time was provided through XSEDE Allocation Grant MCA05S028 and the BlueWaters petascale supercomputer system (UIUC).

## REFERENCES

- (1) Dekker, C. Solid-State Nanopores. *Nat. Nanotechnol.* **2007**, *2*, 209–215.
- (2) Bayley, H. Nanopore Sequencing: From Imagination to Reality. *Clin. Chem.* **2015**, *61*, 25–31.
- (3) Kasianowicz, J. J.; Robertson, J. W.; Chan, E. R.; Reiner, J. E.; Stanford, V. M. Nanoscopic Porous Sensors. *Annu. Rev. Anal. Chem.* **2008**, *1*, 737–766.
- (4) Howorka, S.; Siwy, Z. Nanopore Analytics: Sensing of Single Molecules. *Chem. Soc. Rev.* **2009**, *38*, 2360–2384.
- (5) Haque, F.; Li, J.; Wu, H.-C.; Liang, X.-J.; Guo, P. Solid-State and Biological Nanopore for Real-Time Sensing of Single Chemical and Sequencing of DNA. *Nano Today* **2013**, *8*, 56–74.
- (6) Fennouri, A.; Przybylski, C. d.; Pastoriza-Gallego, M.; Bacri, L.; Auvray, L. c.; Daniel, R. g., Single Molecule Detection of Glycosaminoglycan Hyaluronic Acid Oligosaccharides and Depolymerization Enzyme Activity Using a Protein Nanopore. *ACS Nano* **2012**, *6*, 9672–9678.
- (7) Bacri, L.; Oukhaled, A.; Hémon, E.; Bassafoula, F. B.; Auvray, L.; Daniel, R. Discrimination of Neutral Oligosaccharides through a Nanopore. *Biochem. Biophys. Res. Commun.* **2011**, *412*, 561–564.
- (8) Waduge, P.; Hu, R.; Bandarkar, P.; Yamazaki, H.; Cressiot, B.; Zhao, Q.; Whitford, P.; Wanunu, M. Nanopore-Based Measurements of Protein Size, Fluctuations, and Conformational Changes. *ACS Nano* **2017**, *11*, 5706–5716.
- (9) Li, J.; Fologea, D.; Rollings, R.; Ledden, B. Characterization of Protein Unfolding with Solid-State Nanopores. *Protein Pept. Lett.* **2014**, *21*, 256–265.
- (10) Fologea, D.; Ledden, B.; McNabb, D. S.; Li, J. Electrical Characterization of Protein Molecules by a Solid-State Nanopore. *Appl. Phys. Lett.* **2007**, *91*, 053901.
- (11) Firnkes, M.; Pedone, D.; Knezevic, J.; Döblinger, M.; Rant, U. Electrically Facilitated Translocations of Proteins through Silicon Nitride Nanopores: Conjoint and Competitive Action of Diffusion, Electrophoresis, and Electroosmosis. *Nano Lett.* **2010**, *10*, 2162–2167.
- (12) Talaga, D. S.; Li, J. Single-Molecule Protein Unfolding in Solid State Nanopores. *J. Am. Chem. Soc.* **2009**, *131*, 9287–9297.
- (13) Wanunu, M.; Bhattacharya, S.; Xie, Y.; Tor, Y.; Aksimentiev, A.; Drndic, M. Nanopore Analysis of Individual Rna/Antibiotic Complexes. *ACS Nano* **2011**, *5*, 9345–9353.
- (14) Wanunu, M.; Sutin, J.; McNally, B.; Chow, A.; Meller, A. DNA Translocation Governed by Interactions with Solid-State Nanopores. *Biophys. J.* **2008**, *95*, 4716–4725.
- (15) Squires, A.; Gilboa, T.; Torfstein, C.; Varongchayakul, N.; Meller, A. Chapter Fourteen—Single-Molecule Characterization of DNA–Protein Interactions Using Nanopore Biosensors. *Methods Enzymol.* **2017**, *582*, 353–385.
- (16) Wang, S.; Haque, F.; Rychahou, P. G.; Evers, B. M.; Guo, P. Engineered Nanopore of Phi29 DNA-Packaging Motor for Real-Time Detection of Single Colon Cancer Specific Antibody in Serum. *ACS Nano* **2013**, *7*, 9814–9822.
- (17) Reiner, J. E.; Balijepalli, A.; Robertson, J. W.; Campbell, J.; Suehle, J.; Kasianowicz, J. J. Disease Detection and Management Via Single Nanopore-Based Sensors. *Chem. Rev.* **2012**, *112*, 6431–6451.
- (18) Wanunu, M.; Dadosh, T.; Ray, V.; Jin, J.; McReynolds, L.; Drndić, M. Rapid Electronic Detection of Probe-Specific Micromas Using Thin Nanopore Sensors. *Nat. Nanotechnol.* **2010**, *5*, 807–814.
- (19) Wang, Y.; Zheng, D.; Tan, Q.; Wang, M. X.; Gu, L.-Q. Nanopore-Based Detection of Circulating Micromas in Lung Cancer Patients. *Nat. Nanotechnol.* **2011**, *6*, 668–674.
- (20) Branton, D.; Deamer, D. W.; Marziali, A.; Bayley, H.; Benner, S. A.; Butler, T.; Di Ventra, M.; Garaj, S.; Hibbs, A.; Huang, X.; et al. The Potential and Challenges of Nanopore Sequencing. *Nat. Biotechnol.* **2008**, *26*, 1146–1153.
- (21) Carson, S.; Wanunu, M. Challenges in DNA Motion Control and Sequence Readout Using Nanopore Devices. *Nanotechnology* **2015**, *26*, 074004.
- (22) Venkatesan, B. M.; Bashir, R. Nanopore Sensors for Nucleic Acid Analysis. *Nat. Nanotechnol.* **2011**, *6*, 615–624.
- (23) Wanunu, M. Nanopores: A Journey Towards DNA Sequencing. *Phys. Life Rev.* **2012**, *9*, 125–158.
- (24) Guo, P. The Emerging Field of Rna Nanotechnology. *Nat. Nanotechnol.* **2010**, *5*, 833–842.
- (25) Osada, E.; Suzuki, Y.; Hidaka, K.; Ohno, H.; Sugiyama, H.; Endo, M.; Saito, H. Engineering Rna–Protein Complexes with Different Shapes for Imaging and Therapeutic Applications. *ACS Nano* **2014**, *8*, 8130–8140.
- (26) Ohno, H.; Kobayashi, T.; Kabata, R.; Endo, K.; Iwasa, T.; Yoshimura, S. H.; Takeyasu, K.; Inoue, T.; Saito, H. Synthetic Rna-Protein Complex Shaped Like an Equilateral Triangle. *Nat. Nanotechnol.* **2011**, *6*, 116–120.
- (27) Afonin, K. A.; Bindewald, E.; Yaghoubian, A. J.; Voss, N.; Jacovetty, E.; Shapiro, B. A.; Jaeger, L. In Vitro Assembly of Cubic Rna-Based Scaffolds Designed in Silico. *Nat. Nanotechnol.* **2010**, *5*, 676–682.
- (28) Afonin, K. A.; Cieply, D. J.; Leontis, N. B. Specific Rna Self-Assembly with Minimal Paranemic Motifs. *J. Am. Chem. Soc.* **2008**, *130*, 93–102.
- (29) Afonin, K. A.; Grabow, W. W.; Walker, F. M.; Bindewald, E.; Dobrovolskaia, M. A.; Shapiro, B. A.; Jaeger, L. Design and Self-Assembly of Sirna-Functionalized Rna Nanoparticles for Use in Automated Nanomedicine. *Nat. Protoc.* **2011**, *6*, 2022–2034.
- (30) Afonin, K. A.; Kasprzak, W.; Bindewald, E.; Puppala, P. S.; Diehl, A. R.; Hall, K. T.; Kim, T. J.; Zimmermann, M. T.; Jernigan, R. L.; Jaeger, L.; Shapiro, B. A. Computational and Experimental Characterization of Rna Cubic Nanoscaffolds. *Methods* **2014**, *67*, 256–265.
- (31) Afonin, K. A.; Kasprzak, W. K.; Bindewald, E.; Kireeva, M.; Viard, M.; Kashlev, M.; Shapiro, B. A. In Silico Design and Enzymatic Synthesis of Functional Rna Nanoparticles. *Acc. Chem. Res.* **2014**, *47*, 1731–1741.
- (32) Afonin, K. A.; Lindsay, B.; Shapiro, B. A. Engineered Rna Nanodesigns for Applications in Rna Nanotechnology. *DNA RNA Nanotechnol.* **2013**, *1*, 1–15.
- (33) Bui, M. N.; Brittany Johnson, M.; Viard, M.; Satterwhite, E.; Martins, A. N.; Li, Z.; Marriott, I.; Afonin, K. A.; Khisamutdinov, E. F. Versatile Rna Tetra-U Helix Linking Motif as a Toolkit for Nucleic Acid Nanotechnology. *Nanomedicine* **2017**, *13*, 1137–1146.
- (34) Dibrov, S. M.; McLean, J.; Parsons, J.; Hermann, T. Self-Assembling Rna Square. *Proc. Natl. Acad. Sci. U. S. A.* **2011**, *108*, 6405–6408.
- (35) Guo, P.; Haque, F.; Hallahan, B.; Reif, R.; Li, H. Uniqueness, Advantages, Challenges, Solutions, and Perspectives in Therapeutics Applying RNA Nanotechnology. *Nucleic Acid Ther.* **2012**, *22*, 226–245.
- (36) Guo, P.; Zhang, C.; Chen, C.; Garver, K.; Trottier, M. Inter-Rna Interaction of Phage Phi29 Prna to Form a Hexameric Complex for Viral DNA Transportation. *Mol. Cell* **1998**, *2*, 149–155.
- (37) Guo, S.; Huang, F.; Guo, P. Construction of Folate-Conjugated Prna of Bacteriophage Phi29 DNA Packaging Motor for Delivery of Chimeric Sirna to Nasopharyngeal Carcinoma Cells. *Gene Ther.* **2006**, *13*, 1553.
- (38) Bhatia, D.; Arumugam, S.; Nasilowski, M.; Joshi, H.; Wunder, C.; Chambon, V.; Prakash, V.; Grazon, C.; Nadal, B.; Maiti, P. K.; et al. Quantum Dot-Loaded Monofunctionalized DNA Icosahedra for Single-Particle Tracking of Endocytic Pathways. *Nat. Nanotechnol.* **2016**, *11*, 1112–1119.
- (39) Bhatia, D.; Mehtab, S.; Krishnan, R.; Indi, S. S.; Basu, A.; Krishnan, Y. Icosahedral DNA Nanocapsules by Modular Assembly. *Angew. Chem., Int. Ed.* **2009**, *48*, 4134–4137.
- (40) He, Y.; Ye, T.; Su, M.; Zhang, C.; Ribbe, A. E.; Jiang, W.; Mao, C. Hierarchical Self-Assembly of DNA into Symmetric Supramolecular Polyhedra. *Nature* **2008**, *452*, 198–202.
- (41) Andersen, E. S.; Dong, M.; Nielsen, M. M.; Jahn, K.; Subramani, R.; Mamdouh, W.; Golas, M. M.; Sander, B.; Stark, H.; Oliveira, C. L.; et al. Self-Assembly of a Nanoscale DNA Box with a Controllable Lid. *Nature* **2009**, *459*, 73–76.

- (42) Bujold, K. E.; Hsu, J. C.; Sleiman, H. F. Optimized DNA "Nanosuitcases" for Encapsulation and Conditional Release of Sirna. *J. Am. Chem. Soc.* **2016**, *138*, 14030–14038.
- (43) Chidchob, P.; Edwardson, T. G.; Serpell, C. J.; Sleiman, H. F. Synergy of Two Assembly Languages in DNA Nanostructures: Self-Assembly of Sequence-Defined Polymers on DNA Cages. *J. Am. Chem. Soc.* **2016**, *138*, 4416–4425.
- (44) Liu, Z.; Tian, C.; Yu, J.; Li, Y.; Jiang, W.; Mao, C. Self-Assembly of Responsive Multilayered DNA Nanocages. *J. Am. Chem. Soc.* **2015**, *137*, 1730–1733.
- (45) Yu, J.; Liu, Z.; Jiang, W.; Wang, G.; Mao, C. De Novo Design of an Rna Tile That Self-Assembles into a Homo-Octameric Nanoprism. *Nat. Commun.* **2015**, *6*, 5724.
- (46) Goodman, R. P.; Schaap, I. A.; Tardin, C. F.; Erben, C. M.; Berry, R. M.; Schmidt, C. F.; Turberfield, A. J. Rapid Chiral Assembly of Rigid DNA Building Blocks for Molecular Nanofabrication. *Science* **2005**, *310*, 1661–1665.
- (47) Halman, J. R.; Satterwhite, E.; Roark, B.; Chandler, M.; Viard, M.; Ivanina, A.; Bindewald, E.; Kasprzak, W. K.; Panigaj, M.; Bui, M. N.; Lu, J. S.; Miller, J.; Khisamutdinov, E. F.; Shapiro, B. A.; Dobrovolskaia, M. A.; Afonin, K. A. Functionally-Interdependent Shape-Switching Nanoparticles with Controllable Properties. *Nucleic Acids Res.* **2017**, *45*, 2210–2220.
- (48) Afonin, K. A.; Viard, M.; Koyfman, A. Y.; Martins, A. N.; Kasprzak, W. K.; Panigaj, M.; Desai, R.; Santhanam, A.; Grabow, W. W.; Jaeger, L.; Heldman, E.; Reiser, J.; Chiu, W.; Freed, E. O.; Shapiro, B. A. Multifunctional Rna Nanoparticles. *Nano Lett.* **2014**, *14*, 5662–5671.
- (49) Dao, B. N.; Viard, M.; Martins, A. N.; Kasprzak, W. K.; Shapiro, B. A.; Afonin, K. A. Triggering Rnai with Multifunctional Rna Nanoparticles and Their Delivery. *DNA RNA Nanotechnol.* **2015**, *1*, 27–38.
- (50) Guo, S.; Tschammer, N.; Mohammed, S.; Guo, P. Specific Delivery of Therapeutic Rnas to Cancer Cells Via the Dimerization Mechanism of Phi29 Motor Prna. *Hum. Gene Ther.* **2005**, *16*, 1097–1109.
- (51) Li, H.; Zhang, K. M.; Pi, F. M.; Guo, S. J.; Shlyakhtenko, L.; Chiu, W.; Shu, D.; Guo, P. X. Controllable Self-Assembly of Rna Tetrahedrons with Precise Shape and Size for Cancer Targeting. *Adv. Mater.* **2016**, *28*, 7501–7507.
- (52) Cassinelli, V.; Oberleitner, B.; Sobotta, J.; Nickels, P.; Grossi, G.; Kemper, S.; Frischmuth, T.; Liedl, T.; Manetto, A. One-Step Formation of "Chain-Armor"-Stabilized DNA Nanostructures. *Angew. Chem., Int. Ed.* **2015**, *54*, 7795–7798.
- (53) Kim, H.; Lee, J. S.; Lee, J. B. Generation of Sirna Nanosheets for Efficient Rna Interference. *Sci. Rep.* **2016**, *6*, 25146.
- (54) Stewart, J. M.; Viard, M.; Subramanian, H. K. K.; Roark, B. K.; Afonin, K. A.; Franco, E. Programmable Rna Microstructures for Coordinated Delivery of Sirnas. *Nanoscale* **2016**, *8*, 17542–17550.
- (55) Saleh, O. A.; Sohn, L. L. Direct Detection of Antibody–Antigen Binding Using an on-Chip Artificial Pore. *Proc. Natl. Acad. Sci. U. S. A.* **2003**, *100*, 820–824.
- (56) Wu, H.; Liu, H.; Tan, S.; Yu, J.; Zhao, W.; Wang, L.; Liu, Q. The Estimation of Field-Dependent Conductance Change of Nanopore by Field-Induced Charge in the Translocations of Aunps-DNA Conjugates. *J. Phys. Chem. C* **2014**, *118*, 26825–26835.
- (57) Cai, H.; Wang, Y.; Yu, Y.; Mirkin, M. V.; Bhakta, S.; Bishop, G. W.; Joshi, A. A.; Rusling, J. F. Resistive-Pulse Measurements with Nanopipettes: Detection of Vascular Endothelial Growth Factor C (Vegf-C) Using Antibody-Decorated Nanoparticles. *Anal. Chem.* **2015**, *87*, 6403–6410.
- (58) Wang, Y.; Kecici, K.; Mirkin, M. V.; Mani, V.; Sardesai, N.; Rusling, J. F. Resistive-Pulse Measurements with Nanopipettes: Detection of Au Nanoparticles and Nanoparticle-Bound Anti-Peanut Igy. *Chem. Sci.* **2013**, *4*, 655–663.
- (59) Pevarnik, M.; Schiel, M.; Yoshimatsu, K.; Vlassioux, I. V.; Kwon, J. S.; Shea, K. J.; Siwy, Z. S. Particle Deformation and Concentration Polarization in Electroosmotic Transport of Hydrogels through Pores. *ACS Nano* **2013**, *7*, 3720–3728.
- (60) Holden, D. A.; Hendrickson, G. R.; Lan, W.-J.; Lyon, L. A.; White, H. S. Electrical Signature of the Deformation and Dehydration of Microgels During Translocation through Nanopores. *Soft Matter* **2011**, *7*, 8035–8040.
- (61) Holden, D. A.; Hendrickson, G.; Lyon, L. A.; White, H. S. Resistive Pulse Analysis of Microgel Deformation During Nanopore Translocation. *J. Phys. Chem. C* **2011**, *115*, 2999–3004.
- (62) Yingling, Y. G.; Shapiro, B. A. Computational Design of an Rna Hexagonal Nanoring and an Rna Nanotube. *Nano Lett.* **2007**, *7*, 2328–2334.
- (63) Grabow, W. W.; Zakrevsky, P.; Afonin, K. A.; Chworos, A.; Shapiro, B. A.; Jaeger, L. Self-Assembling Rna Nanorings Based on Rnai/Ii Inverse Kissing Complexes. *Nano Lett.* **2011**, *11*, 878–887.
- (64) Li, J.; Talaga, D. S. The Distribution of DNA Translocation Times in Solid-State Nanopores. *J. Phys.: Condens. Matter* **2010**, *22*, 454129.
- (65) Larkin, J.; Henley, R. Y.; Muthukumar, M.; Rosenstein, J. K.; Wanunu, M. High-Bandwidth Protein Analysis Using Solid-State Nanopores. *Biophys. J.* **2014**, *106*, 696–704.
- (66) Rosenstein, J. K.; Wanunu, M.; Merchant, C. A.; Drndic, M.; Shepard, K. L. Integrated Nanopore Sensing Platform with Sub-Microsecond Temporal Resolution. *Nat. Methods* **2012**, *9*, 487–492.
- (67) Heng, J. B.; Aksimentiev, A.; Ho, C.; Marks, P.; Grinkova, Y. V.; Sligar, S.; Schulten, K.; Timp, G. Stretching DNA Using the Electric Field in a Synthetic Nanopore. *Nano Lett.* **2005**, *5*, 1883–1888.
- (68) Plesa, C.; Ananth, A. N.; Linko, V.; Gülcher, C.; Katan, A. J.; Dietz, H.; Dekker, C. Ionic Permeability and Mechanical Properties of DNA Origami Nanoplates on Solid-State Nanopores. *ACS Nano* **2014**, *8*, 35–43.
- (69) Kim, M. J.; McNally, B.; Murata, K.; Meller, A. Characteristics of Solid-State Nanometre Pores Fabricated Using a Transmission Electron Microscope. *Nanotechnology* **2007**, *18*, 205302.
- (70) Kim, M. J.; Wanunu, M.; Bell, D. C.; Meller, A. Rapid Fabrication of Uniformly Sized Nanopores and Nanopore Arrays for Parallel DNA Analysis. *Adv. Mater.* **2006**, *18*, 3149–3153.
- (71) Gershow, M.; Golovchenko, J. A. Recapturing and Trapping Single Molecules with a Solid-State Nanopore. *Nat. Nanotechnol.* **2007**, *2*, 775–779.
- (72) Wanunu, M.; Morrison, W.; Rabin, Y.; Grosberg, A. Y.; Meller, A. Electrostatic Focusing of Unlabelled DNA into Nanoscale Pores Using a Salt Gradient. *Nat. Nanotechnol.* **2010**, *5*, 160–165.
- (73) Shlyakhtenko, L. S.; Gall, A. A.; Lyubchenko, Y. L. Mica Functionalization for Imaging of DNA and Protein-DNA Complexes with Atomic Force Microscopy. *Methods Mol. Biol.* **2012**, *931*, 295–312.
- (74) Shlyakhtenko, L. S.; Gall, A. A.; Filonov, A.; Cerovac, Z.; Lushnikov, A.; Lyubchenko, Y. L. Silatrane-Based Surface Chemistry for Immobilization of DNA, Protein-DNA Complexes and Other Biological Materials. *Ultramicroscopy* **2003**, *97*, 279–287.
- (75) Phillips, J. C.; Braun, R.; Wang, W.; Gumbart, J.; Tajkhorshid, E.; Villa, E.; Chipot, C.; Skeel, R. D.; Kale, L.; Schulten, K. Scalable Molecular Dynamics with Namd. *J. Comput. Chem.* **2005**, *26*, 1781–1802.
- (76) Best, R. B.; Zhu, X.; Shim, J.; Lopes, P. E.; Mittal, J.; Feig, M.; MacKerell, A. D., Jr Optimization of the Additive Charmm All-Atom Protein Force Field Targeting Improved Sampling of the Backbone  $\phi$ ,  $\Psi$  and Side-Chain X1 and X2 Dihedral Angles. *J. Chem. Theory Comput.* **2012**, *8*, 3257–3273.
- (77) Cruz-Chu, E. R.; Aksimentiev, A.; Schulten, K. Water–Silica Force Field for Simulating Nanodevices. *J. Phys. Chem. B* **2006**, *110*, 21497–21508.
- (78) Yoo, J.; Aksimentiev, A. Competitive Binding of Cations to Duplex DNA Revealed through Molecular Dynamics Simulations. *J. Phys. Chem. B* **2012**, *116*, 12946–12954.
- (79) Batcho, P. F.; Case, D. A.; Schlick, T. Optimized Particle-Mesh Ewald/Multiple-Time Step Integration for Molecular Dynamics Simulations. *J. Chem. Phys.* **2001**, *115*, 4003–4018.

(80) Darden, T.; York, D.; Pedersen, L. Particle Mesh Ewald: An  $N \cdot \log(N)$  Method for Ewald Sums in Large Systems. *J. Chem. Phys.* **1993**, *98*, 10089–10092.

(81) Miyamoto, S.; Kollman, P. A. Settle: An Analytical Version of the Shake and Rattle Algorithm for Rigid Water Models. *J. Comput. Chem.* **1992**, *13*, 952–962.

(82) Andersen, H. C. Rattle: A “Velocity” Version of the Shake Algorithm for Molecular Dynamics Calculations. *J. Comput. Phys.* **1983**, *52*, 24–34.

(83) Martyna, G. J.; Tobias, D. J.; Klein, M. L. Constant Pressure Molecular Dynamics Algorithms. *J. Chem. Phys.* **1994**, *101*, 4177–4189.

(84) Van Beest, B.; Kramer, G. J.; Van Santen, R. Force Fields for Silicas and Aluminophosphates Based on Ab Initio Calculations. *Phys. Rev. Lett.* **1990**, *64*, 1955–1958.

(85) Aksimentiev, A.; Heng, J. B.; Timp, G.; Schulten, K. Microscopic Kinetics of DNA Translocation through Synthetic Nanopores. *Biophys. J.* **2004**, *87*, 2086–2097.

(86) Comer, J.; Dimitrov, V.; Zhao, Q.; Timp, G.; Aksimentiev, A. Microscopic Mechanics of Hairpin DNA Translocation through Synthetic Nanopores. *Biophys. J.* **2009**, *96*, 593–608.